



## Effects of Forbush decreases on clouds determined from PATMOS-x

Matsumoto, Haruka; Svensmark, Henrik; Enghoff, Martin Bødker

*Published in:*  
Journal of Atmospheric and Solar-Terrestrial Physics

*Link to article, DOI:*  
[10.1016/j.jastp.2022.105845](https://doi.org/10.1016/j.jastp.2022.105845)

*Publication date:*  
2022

*Document Version*  
Publisher's PDF, also known as Version of record

[Link back to DTU Orbit](#)

*Citation (APA):*  
Matsumoto, H., Svensmark, H., & Enghoff, M. B. (2022). Effects of Forbush decreases on clouds determined from PATMOS-x. *Journal of Atmospheric and Solar-Terrestrial Physics*, 230, Article 105845. <https://doi.org/10.1016/j.jastp.2022.105845>

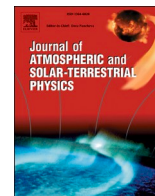
---

### General rights

Copyright and moral rights for the publications made accessible in the public portal are retained by the authors and/or other copyright owners and it is a condition of accessing publications that users recognise and abide by the legal requirements associated with these rights.

- Users may download and print one copy of any publication from the public portal for the purpose of private study or research.
- You may not further distribute the material or use it for any profit-making activity or commercial gain
- You may freely distribute the URL identifying the publication in the public portal

If you believe that this document breaches copyright please contact us providing details, and we will remove access to the work immediately and investigate your claim.



## Research Paper

## Effects of Forbush decreases on clouds determined from PATMOS-x

Haruka Matsumoto<sup>\*</sup>, Henrik Svensmark, Martin Bødker Enghoff

DTUspace, Technical University of Denmark, Denmark

## ARTICLE INFO

## Keywords:

Cosmic rays  
Clouds  
PATMOS-x

## ABSTRACT

This study examines the relationship between cosmic rays and clouds during Forbush decreases (FDs) to understand the cause-effect relationships between cloud microphysics, cloud condensation nuclei (CCN), and ionisation in the atmosphere. The results of a Monte Carlo analysis of cloud parameters during FDs, which were obtained using newly calibrated satellite data (Pathfinder Atmospheres Extended (PATMOS-x)) from 1978 to 2018, show the connections between some cloud parameters and FDs. For context, FD is the event where the number of cosmic rays arriving in the atmosphere decreases and recovers over several days. Other studies have shown that FDs impacted the cloud fraction, aerosol optical depth, CCN, water content, and cloud effective radius ( $r_{eff}$ ) in the atmosphere. Using the Monte Carlo analysis, nine atmospheric parameters from the dataset were evaluated and exhibited a significant response to FDs. Each added FD event (after the first event) reduces the noise, but only the strongest events add a significant signal (exceptionally when the 2nd and 5th rank FD data are added, the signal/noise ratio dropped due to a change in the satellite version). We found that cloud fraction shows statistically significant signals following FDs at an achieved significance level of 0.33%. Cloud emissivity also showed highly significant signals from the analysis; however, these cannot be classified as physical causes of FDs since the response starts a week before the FDs. In contrast, the cloud optical depth, integrated total cloud water over the entire column, and  $r_{eff}$  did not show any significant signals in the frameworks of the applied methods. The top of the atmosphere brightness temperatures (TABTs) at nominal wavelengths of 3.75, 11.0, and 12.0  $\mu\text{m}$  were analysed again along with surface BTs and showed significant signals. The estimated changes in the BT were determined using a radiative transfer model (Fu-Liou model) and showed consistent results with the observed changes in cloud parameters during FD events. Among the analysed several atmospheric/cloud/aerosol parameters, cloud fraction and TABT at nominal wavelengths of 3.75, 11.0, and 12.0  $\mu\text{m}$  are the only parameters depicting a statistically significant and correct-phase response to FDs.

## 1. Introduction

The interactions between aerosols and clouds are not fully understood yet. They affect each other in the atmosphere during cloud formation, particle nucleation process, or aerosol number concentration. Ions have been shown to promote the formation and growth of aerosols and are thus one of the key factors elucidating the aerosol-cloud relationship (Wagner et al., 2017; Kirkby et al., 2016; Tomicic et al., 2018; Lehtipalo et al., 2016). Initially, the relationship between cosmic ray clouds, aerosols, and other parameters was investigated over long timescales of at least several years. Long-term studies are crucial for a deeper understanding of the Earth's climate. Meanwhile, separating the effects of galactic cosmic rays (GCRs) from other factors is difficult and can potentially change cloud parameters, such as solar UV effects, atmospheric circulation changes, and trends in other climate effects. These

can sometimes appear as noise and conceal small signals by GCRs because of close correlation. (Todd and Kniveton, 2004; Voiculescu et al., 2006). Hence, another approach is adopted here to distinguish the noise generated on a long timescale with potential signals from GCRs. The sudden reduction of GCRs coming to Earth is known as Forbush decreases (FDs). FDs are natural temporal variations in cosmic radiation on a timescale of a few days, with a recovery time of about eight to 10 days (Forbush, 1937). FDs are caused by heliospheric magnetic shock and turbulent magnetic fields, following a coronal mass ejection (CME) from the Sun that scatters GCRs. In this study, we investigated the behaviour of clouds during short-term changes in atmospheric ionisation caused by GCRs controlled via solar activity. Changes in the GCR flux, 10.7 cm solar radio flux, soft X-rays, ultraviolet radiation, and cloud cover using satellite cloud data sets have previously been compared (Tsubota, 1995; Udelhofen and Cess, 2001). Monthly means

<sup>\*</sup> Corresponding author.

E-mail address: [harmat@space.dtu.dk](mailto:harmat@space.dtu.dk) (H. Matsumoto).

<https://doi.org/10.1016/j.jastp.2022.105845>

Received 25 June 2021; Received in revised form 24 February 2022; Accepted 26 February 2022

Available online 10 March 2022

1364-6826/© 2022 The Authors. Published by Elsevier Ltd. This is an open access article under the CC BY license (<http://creativecommons.org/licenses/by/4.0/>).

of cloud cover at different altitudes, as defined by the pressure (high: <440 hPa, middle: 440–680 hPa, low: >680 hPa) measured from the International Satellite Cloud Climatology Project (ISCCP) and Climax Neutron Monitor data from 1980 to 1995, were also investigated. A correlation between cloud cover at low altitudes and GCR fluxes was observed, and the geographical region factor supported ideas that the cosmic ray effect is varied for each region (Marsh and Svensmark, 2000; Voiculescu and Usoskin, 2012). The lack of correlation with cloud cover at higher altitudes is not fully understood. Todd and Kniveton (2001) found strong signals between the GCR flux, global precipitation, and precipitation efficiency over the global ocean at mid to high latitudes from 1979 to 1999. In other studies, a relationship between cosmic rays and cloudiness was only observed for marine clouds at mid-latitudes (Kristjansson & Kristiansen, 2000; Voiculescu et al., 2013). Sun and Bradley (2002) found no conclusive relationship between cosmic rays and cloud cover at low altitudes in both ground and satellite-based cloud data. Similarly, Laken and Čalogović (2011) found no significant link between cloud cover in the low (0.0–3.2 km), middle (3.2–6.5 km), and high ( $\geq 6.5$  km) troposphere and at different latitudes with changes in the total solar irradiance (TSI), GCRs, or UV flux.

These studies inspired further research to deepen the understanding of how ionisation by GCRs affects aerosol behaviour, which are the precursors to clouds (Tinsley and Heelis, 1993; Nicoll and Harrison, 2010). An experimental study was conducted on the role of ionisation in a controlled reaction chamber, replicating the atmospheric conditions. This experiment showed that the amount of newly produced aerosol particles ( $d \sim 3$  nm) was proportional to negative ion density (H. Svensmark et al., 2006). In the real atmosphere, however, the effective size of cloud condensation nuclei (CCN) is typically larger than 50 nm. Therefore, another project using an  $8\text{ m}^3$  reaction chamber (SKY2) was conducted to empirically investigate the effects of ions on CCN formation. This experiment provided supportive evidence that an ion mechanism facilitates growth of newly nucleated aerosols to CCN sizes in the pure air (Svensmark et al., 2013). The Cosmics Leaving Outdoor Droplets (CLOUD) experiment has provided direct measurements of molecular compositions from single molecules to stable compositions, thereby providing further details regarding the effects of ionising radiations on aerosol formation (Kirkby et al., 2011). Several studies have revealed the support ionisation effects on cloud physics (Tinsley, 2000; Tinsley and Deen, 1991). A subsequent study (H. Svensmark et al., 2017) revealed the physical mechanism of how ions affect the growth of aerosols in various stages (from nucleation to those exhibiting sizes  $>20$  nm), demonstrating an agreement between theory and experiments.

The effect of FDs has been studied using different materials and methodologies in previous works. Svensmark et al. (2009) as well as Pudovkin and Veretenenko (1995) found a connection between several parameters: Cloud water content from the Special Sensor Microwave/Imager (SSM/I), cloud cover from the moderate resolution imaging spectroradiometer (MODIS) and ISCCP, and aerosol optical depth from the aerosol robotic networks (AERONET) during 26 FD events. Subsequently, a parameter carrying information on the liquid water cloud fraction (LCF) was reanalysed by Laken et al. (2009), who concluded that there was no correlation with FD events. Connections among the cloud index (CI), cloud occurrence frequency (Occ), extinction data (Ext), and climax neutron monitor data (CNM) were investigated over six FD events; however, no link between GCRs and clouds was found in terms of CI, Occ, or latitude (Rohs et al., 2010). There was insufficient evidence for correlation of global cloud cover and GCR in an analysis using selected FD data based on the reduction of GCRs with energies of 10 GeV (Čalogović et al., 2010). In another instance, the diurnal temperature range (DTR), which is anti-correlated with cloudiness, has been used for a superposed epoch analysis on a set of FDs. The results showed a significant connection but were restricted to high-amplitude FDs (Dragić et al., 2011). A recent study by Svensmark et al. (2016) using a Monte Carlo analysis indicated statistically significant results during FD events, for aerosols from AERONET, liquid water

content from SSM/I, total number of high and middle infrared-detected clouds over oceans from ISCCP, and cloud effective emissivity, cloud optical thickness with liquid phase, liquid water contents, cloud fraction, and liquid cloud effective radius from MODIS. The Earth's average net radiative balance change (median value:  $1.2\text{ W/m}^2$ ) has also been observed using the CERES satellite observations during FDs (Svensmark et al., 2021).

This research presents an extension of the work by Svensmark et al. (2016) using different cloud data sets from PATMOS-x, covering the time period from 1978 to 2018. This will provide a more thorough understanding of the relationships between solar activity, cosmic rays, clouds, aerosols, and other parameters. By studying natural climate variations, the impact of human-made climate change can be constrained further. The overall objective of this research is to investigate the PATMOS-x data set over a timescale of 36 days whenever FD events occurred and evaluate the significance level of these signals using a Monte Carlo analysis, which was similar to that used by Svensmark et al. (2016). If the PATMOS-x data set also exhibits a significant result for FDs in relation to the investigated parameters, it will increase the significance of the previously observed effects of galactic cosmic rays on clouds and aerosols. Additionally, previously ignored parameters have been added to the investigation, and the results are presented. The signals of some of the cloud parameters have been used in a radiative transfer model, and the output is compared with an analysis of brightness temperatures (BTs) during FDs.

## 2. Data

### 2.1. Cloud record from the PATMOS-x satellite

This study uses data from the National Oceanic and Atmospheric Administration (NOAA) satellites, primarily NOAA-15. The NOAA satellite series started with the Polar Operational Environmental Satellites (POES) in 1970; PATMOS-x is a project aimed at improving the calibration techniques for cloud parameters of the NOAA data sets, the Geostationary Operational Environmental Satellite (GOES), and the European Organisation for the Exploitation of Meteorological Satellites (EUMESAT) (Heidinger et al., 2014). These satellites circle the Earth 14 times per day, allowing for complete global coverage twice per day in a sun-synchronous orbit. An Advanced Very High Resolution Radiometer (AVHRR) sensor is active on two satellites in opposite orbits: one descending on the moonlit side and one ascending on the sunlit side of the Earth. This double coverage ensures that the entire Earth is observed every 6 h. AVHRR is a passive multi-channel scanning radiometer monitoring the reflected or emitted radiation in the visible and infrared portions of the electromagnetic spectrum of the same area of Earth's surface with the corresponding channel. There are 3 AVHRR generations, and AVHRR/1 series has four channels (0.58–0.68, 0.725–1.1, 3.55–3.93, and 10.5–11.5  $\mu\text{m}$ ) that have been operated since 1978 on NOAA-6/8/10. Next-generation AVHRR/2 series has an additional channel (11.5–12.5  $\mu\text{m}$ ) and exhibits a minor change for one channel (from 10.5 to 11.5 to 10.3–11.3  $\mu\text{m}$ ) since 1981 on NOAA-7/9/11/12/13/14. The AVHRR/3 series added a channel at 1.58–1.64  $\mu\text{m}$  on NOAA-15/16/17/18/19 and all Meteorological Operational (METOP) satellites since 1998 (<https://earth.esa.int/eoga/way/missions/noaa>). PATMOS-x offers 22 atm products. In this study, we used cloud emissivity, cloud optical thickness (COT),  $r_{eff}$ , cloud area fraction computed over a  $3 \times 3$  array, cloud liquid water path (LWP), top of the atmosphere brightness temperature (TABT) at nominal wavelengths of 3.75, 11, and 12  $\mu\text{m}$ , and surface BT. The parameters are shown in Table 1 and explained in the Results section.

### 2.2. GCR observation from neutron monitors

Cosmic rays have been routinely monitored since 1951. Ground-based neutron monitors provide recordings of the secondary radiation

**Table 1**  
PATMOS-x parameters.

Parameter (unit)	PATMOS-x Parameter Name
$\epsilon$ (-)	Convective cloud longwave emissivity atmosphere
$\tau$ (-)	Optical thickness due to cloud
$r_{\text{eff}}$ ( $\mu\text{m}$ )	Effective radius of cloud condensed water particles at cloud top
CF (-)	Cloud area fraction
LWP ( $\text{g}/\text{m}^2$ )	Integrated total cloud water over whole column
$TABT_{3.75}$ (K)	Top of atmosphere brightness temperature at the nominal wavelength of 3.75 $\mu\text{m}$
$TABT_{11}$ (K)	Top of atmosphere brightness temperature at the nominal wavelength of 11.0 $\mu\text{m}$
$TABT_{12}$ (K)	Top of atmosphere brightness temperature at the nominal wavelength of 12.0 $\mu\text{m}$
BT (K)	Surface brightness temperature

in the atmosphere related to primary cosmic rays. The energy of the penetrating cosmic rays varies across latitudes (cut-off rigidity). First, these primary cosmic rays penetrate the geomagnetic field and become secondary cosmic rays, thereby resulting in a cascade of new particles that, among other things, ionise the atmosphere. This study aims to investigate FD effects which cause sudden decreases in the number of cosmic rays on clouds through reduced ionisation; the primary cosmic ray spectrum that passes through the atmosphere is crucial. In this study, we used data from different neutron monitors for calculating the primary cosmic spectrum changes to determine the changes in ionisation throughout Earth's atmosphere, thereby calculating the strength of the FDs in Svensmark et al. (2016). The reason for the usage of the FD strength based on atmospheric ionisation changes caused by cosmic ray spectrum is that the ionisation of the lower atmosphere change impacts the atmosphere/cloud/aerosol. Thus, determining the FD strength orders based on ionisation is important for investigating the effects of cosmic rays on the atmosphere/cloud/aerosol from all other factors, such as the nucleation process or aerosol particle growth affected by ions. However, this will not produce the same results with the standard definition of FD, for example the Space Weather Prediction Centre (SWPC) in IZMIRAN data of FD magnitude for particles with 10 GV rigidity (%) is shown in Table 2 Svensmark et al. (2016) created a list of the FD events' strengths based on their impact on atmospheric ionisation by modelling the ionisation changes caused by the cosmic ray spectrums. FD events are extracted using a threshold of 7% change of fluxes in cosmic rays in the South Pole neutron monitor between 1989 and

2005 as seen in Table 2. Neutron monitor data are from 130 ground-based neutron monitor stations. Multiple cosmic rays' observations are necessary since a change by a FD cannot be determined because response is dependent on the altitude and geomagnetic position in each monitor.

The percentage of ion production decrease was calculated at a latitude of approximately  $45^\circ$  and a cut-off rigidity of 5 GV. U.S. standard atmosphere was used to derive the absolute ion production as a function of height in the atmosphere (Fig. 3 in Svensmark et al., (2016)). In this study, we used the percentage of ion-production change from 0 to 3 km. The cosmic ray flux and the percentage decrease in ion production relative to the decrease in cosmic rays from a solar maximum to a solar minimum over a solar cycle for cycle numbers 21–23 are described in Table 2 (Svensmark et al., 2016). Thus, for example, the 119% decrease in Table 2 implies that for the FD event (October 31, 2003), ion production decreased by 19% more when the change from a solar maximum to a solar minimum over solar cycles number 21–23 is set to 100%. Average ion production change is 0.3 [ion-pairs/s  $\text{cm}^3$ ] over 0–3 km (average ion production at solar maximum is 1.1 and average ion production at solar minimum is 1.4 [ion-pairs/s  $\text{cm}^3$ ]). The change in ionisation is used instead of NM count rates because the theory investigated works through atmospheric ionisation. The FDs' strengths from Table 2 are used for the analysis of the PATMOS-x data set. We also checked FD events from 1978 to 1986, which are not included in Table 2, from Svensmark et al. (2016); accordingly, two events strong enough to compare with the top five strongest FD events are shown in Table 2. These events occurred on July 14, 1982 and May 18, 1981. The event in 1982 cannot be used for the analysis because the aerosol distribution in the atmosphere was affected by volcanic activity that year, as observed from the Mauna Loa Apparent Transmission record (<https://esrl.noaa.gov/gmd/grad/mloapt.html>). Furthermore, the event in 1981 cannot be included in the analysis because the data are only available from the NOAA 6 satellite with AVHRR/1. As such, for our analysis, we used the data from AVHRR/2 and 3 because AVHRR/1 does not have the channel for 11.5–12.5  $\mu\text{m}$ , which gives information concerning the sea surface temperature. Furthermore, TABT at 12  $\mu\text{m}$  is an essential factor to derive the surface BT and other cloud parameters in calibration.

We calculated the signal/noise ratio as a function of the number of added FD events from Table 2 (Fig. 1). Thus, the  $TN_{FD}$  ranges from one to 15. The signal ( $S_{TN_{FD}}$ ) was calculated via the method used for finding the integrated signal (Eq. (1)), and the noise ( $N_{TN_{FD}}$ ) is calculated using

**Table 2**

Fifteen strongest FD events from 1987 to 2007, according to Svensmark et al. (2016). The magnitude of the FD rank order is presented in the first column. Each date of minimum cosmic ray flux is shown in the second column. The third column shows the percentage decrease in ion production owing to FDs relative to the decrease in cosmic rays from solar maximum to solar minimum over a solar cycle (0.3 [ion-pairs/s  $\text{cm}^3$ ]). Parameters A and Y are obtained by the power law fit in  $\delta n_k = -A_k P^{Y_k}$  ( $\delta n_k$ : relative change of the primary spectrum for a sample FD event.  $A_k$ : amplitude.  $P^{Y_k}$ : measured in gigavolts with  $Y_k$  is determined by least squares fit. The strong FD event of 31 October 2003 shows the following parameters:  $A = 229$  and  $Y = -0.87$  (Svensmark et al., 2016). The change from solar maximum to solar minimum is represented by these parameters:  $A = 336$  and  $Y = -1.10$ ). Fifth column shows an upper/lower uncertainty in A. The available PATMOS-x satellite for each FD is noted in the seventh column (after the 6th rank of FD event, it shows only the satellite used for signal/noise ratio analysis). After 2007, strong FD has not occurred. The last column shows the Space Weather Prediction Centre (SWPC) in IZMIRAN data of FD magnitude for particles with 10 GV rigidity.

Order	Date	Decrease (%)	A	$\pm \delta A$	Y	Available satellite	IZMIRAN:MagnM(%)
1	October 31, 2003	119	229	10/9	$0.87 \pm 0.02$	NOAA15,16,17	28 (October 29, 2003)
2	June 13, 1991	87	121	4/4	$0.74 \pm 0.01$	NOAA11	20.4 (June 12, 1991)
3	January 19, 2005	83	273	16/15	$1.09 \pm 0.02$	NOAA15,16,17	10.4 (January 21, 2005)
4	September 13, 2005	75	233	34/33	$1.07 \pm 0.04$	NOAA15,16,17	13.2 (September 11, 2005)
5	March 15, 1989	70	93	14/12	$0.72 \pm 0.06$	NOAA11	20.4 (March 13, 1989)
6	July 16, 2000	70	131	7/7	$0.86 \pm 0.02$	NOAA14	13.5 (July 15, 2000)
7	April 12, 2001	64	153	12/1	$0.96 \pm 0.03$	NOAA15	13.7 (April 11, 2001)
8	October 29, 1991	56	83	4/4	$0.76 \pm 0.02$	NOAA11	17.8 (October 28, 1991)
9	July 9, 1991	54	84	4/4	$0.78 \pm 0.02$	NOAA11	10.5 (July 8, 1991)
10	November 29, 1989	54	173	13/12	$1.08 \pm 0.03$	NOAA11	15.2 (November 27, 1989)
11	November 10, 2004	53	95	8/8	$0.84 \pm 0.04$	NOAA15	8.6 (November 9, 2004)
12	September 26, 2001	50	203	16/15	$1.18 \pm 0.03$	NOAA15	8.9 (September 25, 2001)
13	March 25, 1991	48	82	15/13	$0.82 \pm 0.07$	NOAA13	22.1 (March 24, 1991)
14	July 17, 2005	47	147	14/13	$1.07 \pm 0.04$	NOAA15	4.1 (July 16, 2005)
15	September 25, 1998	45	123	45/33	$1.01 \pm 0.14$	NOAA11	8.7 (September 24, 1998)

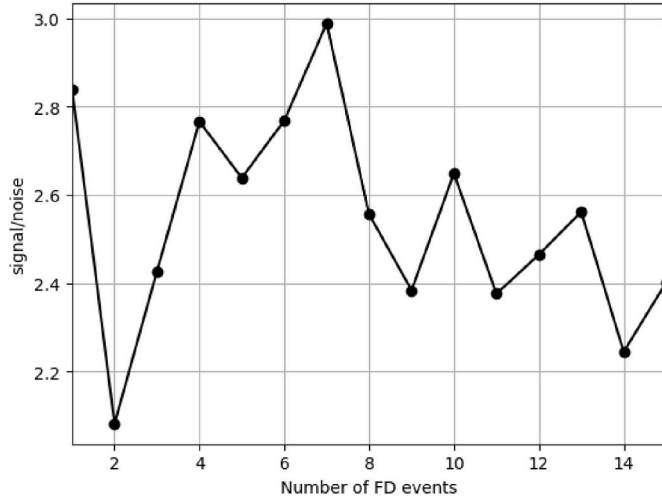


Fig. 1. Signal/noise ratio for the number of added FDs from 1st to 15th rank. Parameter: cloud fraction.

10,000 random samples from the reference time series (Eq. (2)). First, the strongest FD is used and stored as an integrated signal. Then, the second strongest FD time series is added to the strongest FD event and another integrated signal is calculated and stored. This addition process is continued until the 15th rank FD event. Each added event reduces the noise, but only the strongest events contribute to any significant signal. When the 2nd and 5th rank FD data are added, the signal/noise ratio declined from the 1st to 7th FD events. These ratio descents occurred when FD events from NOAA11 were added. This may indicate that NOAA11 has an irregular response to detection of cloud parameters, since this satellite is the oldest version among other satellites used for this analysis. When over 7 FD events are added, the signal/noise ratio decreases as the events become too weak. Therefore, the analysis is focused on the five strongest FDs (Svensmark et al., 2016). Here,  $N_{FD}$  ranges from 1 to 15.

$$S_{TN_{FD}} = \sum_{i=1}^{N_{FD}} F_i(t) w_i \quad (1)$$

( $F_i(t)$ : FD unit (36 days) with index  $i$  for sample unit).

$\overline{BS_j}$  is mean value of  $BS_j$ .

$$N_{N_{FD}} = \left( \frac{1}{N_B} \sum_{j=1}^{N_B} BS_j - \overline{BS_j} \right)^2 \quad (2)$$

( $N_B$ : Number iteration of random sampling.  $BS_j$ : Monte Carlo analysis sample unit.)

### 3. Methods

The data processing and Monte Carlo analysis methods conducted in this project are described below. Used terms are defined in Table 3.

Global data analysis: The original data set ( $m_{xy}$ ) was obtained using a  $0.1^\circ \times 0.1^\circ$  grid cell with an  $1800 \times 3600$  matrix, where  $x$  is the longitude axis from 1 to 3600 and  $y$  is the latitude axis from 1 to 1800.

First, the longitude average ( $\overline{m_y}$ ) was calculated as  $\frac{\sum_{x=1}^{3600} m_{xy}}{3600}$ . To generate a daily global weighted average for each parameter  $\overline{m}$ , a latitudinal area correction was applied to Eq. (3). The weighted averages of the ascending and descending datasets were calculated separately and unified later.

Data points with over 30% of the global grid data missing were excluded from the analysis.

Table 3  
Terms and definitions.

Term	Definition
$\overline{m}$	Daily global weighted average for each parameter
$m$	Daily data for each grid
$N_B$	Number iteration of random sampling
$d$	Denotation of time
$t$	time [day]
$F(t)$	FD unit (36 days)
$U(t)$	Random sample unit (36 days)
$w_i$	Weight coefficient from FD event's strength
$FD_j$	Strength of an FD event
$N_{FD}$	The number of FD event
$FW(t)$	Weighted sum of the FD units
$B_{ij}(t)$	Monte Carlo analysis sample unit
$i$	Denotation of sample unit
$j$	Monte Carlo analysis sample number
$BW_j(t)$	Monte Carlo analysis sample unit, consisting of $N_{FD}$ sample units

$$\overline{m} = \frac{\sum_{y=1}^{1800} \overline{m_y} \cos\left(\frac{\pi}{180}\theta_y\right)}{\sum \cos\left(\frac{\pi}{180}\theta_y\right)} \quad (3)$$

( $\theta_y$  is latitude from 0 to  $180^\circ$  with a  $0.1^\circ$  interval.)

Monte Carlo analysis (Efron and Tibshirani, 1994): To evaluate the signal's significance during FDs, 10,000 ( $N_B$ ) random 36-day time series were formed, following the same procedure as that adopted by Svensmark et al. (2016) using random sampling with the replacement method. A date,  $t_0$ , is defined as the date of minimum cosmic ray flux during the FD; time series is described as  $t_d$ , where  $d$  is between  $-16$  and  $19$ . Therefore, the total number of days is 36 ( $t = [t_0 - 16, t_0 + 19]$ ). The entire reference time series is denoted as  $G(t)$ , and any time series containing an FD event is defined as an FD unit,  $F(t)$ . We used the entire data set from October 26, 1998 to December 31, 2018. The random sample 36-day time series from  $G(t)$  is:

$$U(t) = x(t_{-16}), x(t_{-15}), \dots, x(t_{19}) \quad (4)$$

The 36-day time series including an FD event is:

$$F(t) = x(t_{-16}), x(t_{-15}), \dots, x(t_{19}) \quad (5)$$

If over five days of data points in a  $U(t)$  were missing, the time series  $U(t)$  was excluded from the analysis. When the missing data were below five days, a linear trend between  $t_{-16}$  and  $t_{19}$  was calculated using the least squares method, thereby ignoring the missing data points. Interpolated data were linearly substituted for the missing data points between bounding points. After this process, the trend was removed from the 36-day time series. For example, seasonal temperature trends or solar cycles are approximately linear on a 36-day time scale and can thus be removed.

The strongest FD events, according to Table 2, are superposed. Each event can be given different weights. Three weight distributions were used by Svensmark et al. (2016), but no critical differences were found in the results when using different weights. Therefore, we use the weight from Eq. (6), where the weight of each FD is based on the total strength of the FD from Table 2.

$$w_i = \frac{FD_j(\text{strength})}{\sum_{j=1}^{N_{FD}} FD_j(\text{strength})} \quad (6)$$

$$w_i = \frac{1}{N_{FD}} \text{ for } i = [1, 2, \dots, N_{FD}] \quad (7)$$

( $FD_j$  is the strength of an FD event;  $N_{FD}$  is the number of FD events.)

The weighted sum of the FD units then becomes the following:

$$FW(t) = \sum_{i=1}^{N_{FD}} F_i(t) w_i \quad (8)$$

It is believed that the growth of new aerosol particles into CCN in the atmosphere lasts from a few days to a week, depending on atmospheric conditions (Kulmala et al., 2004). After an FD event occurs, the number of cosmic rays in the atmosphere suddenly decreases and then gradually recovers after 1–2 weeks. To evaluate the signal during an FD, examinations performed at either a maximum or minimum peak value are not sufficient as these values can be influenced by daily fluctuations. As such, effects visible in the data for at least a week after the FD event has occurred should be appropriately considered. Therefore, we integrate the signal by using the time from  $t_a = t_0 + 1$  to  $t_b = t_0 + 9$ , where  $t_0$  is the day of the minimum GCR. In contrast, Svensmark et al. (2016) used  $t_0 + 3$  and  $t_0 + 13$ . A few days difference in an integrated area does not critically affect the results, as the peak part of the signal is commonly included.

The final step is to determine the performance of statistical analysis, which in turn is used to investigate the significance level of a signal for each parameter in the prepared data set. The Monte Carlo analysis is a method used for assigning measures of accuracy to statistical estimates. The procedure has been explained in detail by following the method used by Svensmark et al. (2016) and Efron and Tibshirani (1994).

$B_{ij}(t)$  represents the Monte Carlo analysis sample permutation of the  $F_i(t)$  series. Here,  $i$  denotes the sample unit number (1, 2, ...,  $N_{FD}$ ), and  $j$  is the sample number (1, 2, ...,  $N_B$ ). In the case with PATMOS-x,  $N_{FD}$  is five since five FD events were used, and  $N_B$  is set to 10,000 to achieve sufficient statistical reliability. The weights ( $w_i$ ) are applied to each sample unit as follows:

$$BW_j(t) = \sum_{i=1}^{N_{FD}} B_{ij}(t)w_i \quad (9)$$

( $BW_j(t)$  is the sample unit, consisting of  $N_{FD}$  sample units, such that it corresponds to the collection of FD units.) The period to integrate is determined by the selected day  $t_a$  and  $t_b$ , which is decided according to signal duration:

$$BS_j = BW_j(t_1), \dots, BW_j(t_2) = \sum_{t=t_a}^{t_b} BW_j. \quad (10)$$

The test statistic is defined as the difference between the measured value for the time series and the expectation values of the  $N_B$  samples:

$$DBW_j(t) = BW_j(t) - \frac{1}{N_B} \sum_{j=1}^{N_B} BW_j(t) \quad (11)$$

For the integrated data points:

$$DBS_j = BS_j - \frac{1}{N_B} \sum_{j=1}^{N_B} BS_j \quad (12)$$

The FD units have undergone the same process:

$$XFW(t) = FW(t) - \frac{1}{N_B} \sum_{j=1}^{N_B} BW_j(t) \quad (13)$$

The integrated signal is:

$$XFS = FS - \frac{1}{N_B} \sum_{j=1}^{N_B} BS_j \quad (14)$$

Finally, the achieved significance level (ASL) is calculated from the samples (Efron and Tibshirani, 1994). Thus, an achieved significance level of 1% implies that 1% of the random samples from the reference data with a long-time scale (from 1979 to 2018) can appear beyond the change value of the FD event. It also indicates the possibility of the FD event level not occurring often. Therefore, the ASL implies that the confidence level is 99% and significance level is 1%:

$$ASL_{Boot}(t) = 1 - \frac{\text{Number of measurements } DBW_j(t) \geq XFW(t)}{N_B} \quad (15)$$

For integrated signals:

$$ASL_{Boot} = 1 - \frac{\text{Number of measurements } DBS_j \geq XFS}{N_B} \quad (16)$$

Although data from several satellites have been used in the time series, including an FD, we have used only NOAA 15 data from 1998 to 2018 ( $G(t)$ ) for the Monte Carlo noise analysis. The scatter plot and histogram shown in Fig. 2 describe the variability of PATMOS-x from satellites NOAA 11, 15, 16, and 17, which use the same AVHRR instrument to detect clouds. The NOAA 15 shows the largest standard deviation, and as this is used as a primary data set for the Monte Carlo analysis test, the significance level of eventual signals is evaluated under the most demanding conditions.

Note that as all satellite periods covering FDs are used to detect signals; thus, there are sometimes multiple satellites covering the same FD, implying that there are 11 observations in total during the five strongest FDs (Table 2). These 11 FD observations are not independent events, as they refer to three different satellites viewing the same FDs for three events, which are FD ranks 1, 3, and 4. We compared NOAA15, 16, and 17 satellites covering the same FDs for strength ranks 1, 3, and 4 with different parameters. This is shown in Figs. 3–5 (each figure shows a single FD event). Cloud emissivity and cloud fractions computed over a  $3 \times 3$  array are similar for all three satellites. However, other parameters vary more, especially data from NOAA 15 satellite which exhibit more variability than others. The daily sigma was calculated from 10,000 randomly sampled 36-day data sets, whereby the sigma level is noted in figures with dashed lines. This result is observed owing to the removal of the linear trend of each time series, which causes some parts of the data sets to be moved more than others; it is most evident in data sets with high uncertainty like AOT in Fig. 6.

A weighted average of the five strongest events is calculated by using the strength from Table 2 as the weight for each. The test parameters are noted in Table 4. For the superposition, we used only one satellite for each FD event, but we tested all possible different combinations of satellites using five FD events, as seen in Figs. 3–5 and Table 5. The second and fifth strongest FD events are covered only by NOAA 11. Thus, there is no option for other satellites to obtain data during these FD events. For other FD events, there are only three combinations of FD ranks (1, 3, and 4) and NOAA15, 16, and 17 satellites. The results are shown in Fig. 6. For the next step, a Monte Carlo analysis is applied for these different satellite combinations. Details for the Monte Carlo analysis test parameters are shown in Table 6. Weight coefficient ( $w_i$ ) from Eq. (6), which considers the strength of an FD and an equal weighting of the  $F(t)$ , was used. No significant difference between weights from Eqs. (6) and (14) was observed; thus, we used  $w_i$  from Eq. (6) in the following analysis. The Monte Carlo analysis results are summarised with ASL values in Table 6. In the result section, we used NOAA 15 and 11 satellites for discussion because the reference data for calculation of  $\sigma$  and random sampling in the Monte Carlo analysis both originate from NOAA 15. This also implies that the analysis to investigate signals from FD has been conducted with the noisiest reference (see Fig. 2).

## 4. Results

### 4.1. Cloud emissivity

Cloud emissivity is defined as the ratio of the actual emission by a cloud to the emission of a black body at the same temperature according to the Planck function. Cloud parameters, such as cloud optical thickness and droplet size, change this emissivity. An optically thick cloud can be interpreted as a blackbody that emits radiance near the cloud top. In contrast, optically thin clouds are considered more transparent for infrared wavelengths. Aerosols increase the long-wave (LW) emissivity of thin clouds in the upward and downward directions (Garrett et al., 2002). Cloud emissivity at a nominal wavelength of 11  $\mu\text{m}$  was determined using the Algorithm Working Group Cloud Height Algorithm

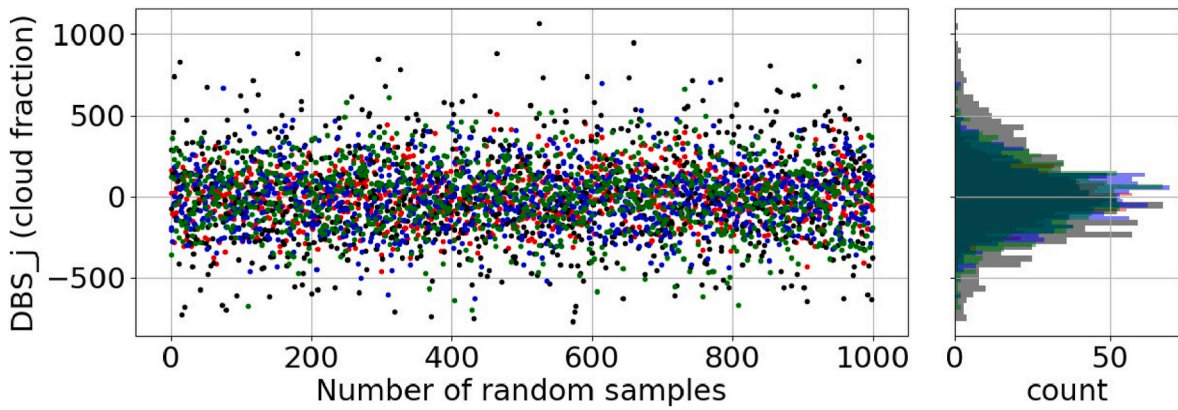


**Fig. 2.** Integrated data points ( $DBS_j$ ) of the cloud fraction parameter from 1000 random samples using raw measurement data from the NOAA 11,15,16, and 17 satellites. Left: Scatter plot with NOAA 11 (red), NOAA15 (black), NOAA16 (blue), and NOAA17 (green). Standard deviation values are 157, 299, 190, and 207, respectively. Right: Composed histograms with NOAA 11 (red), NOAA15 (black), NOAA16 (blue), and NOAA17 (green) in translucent style. The total number of bins is 50.

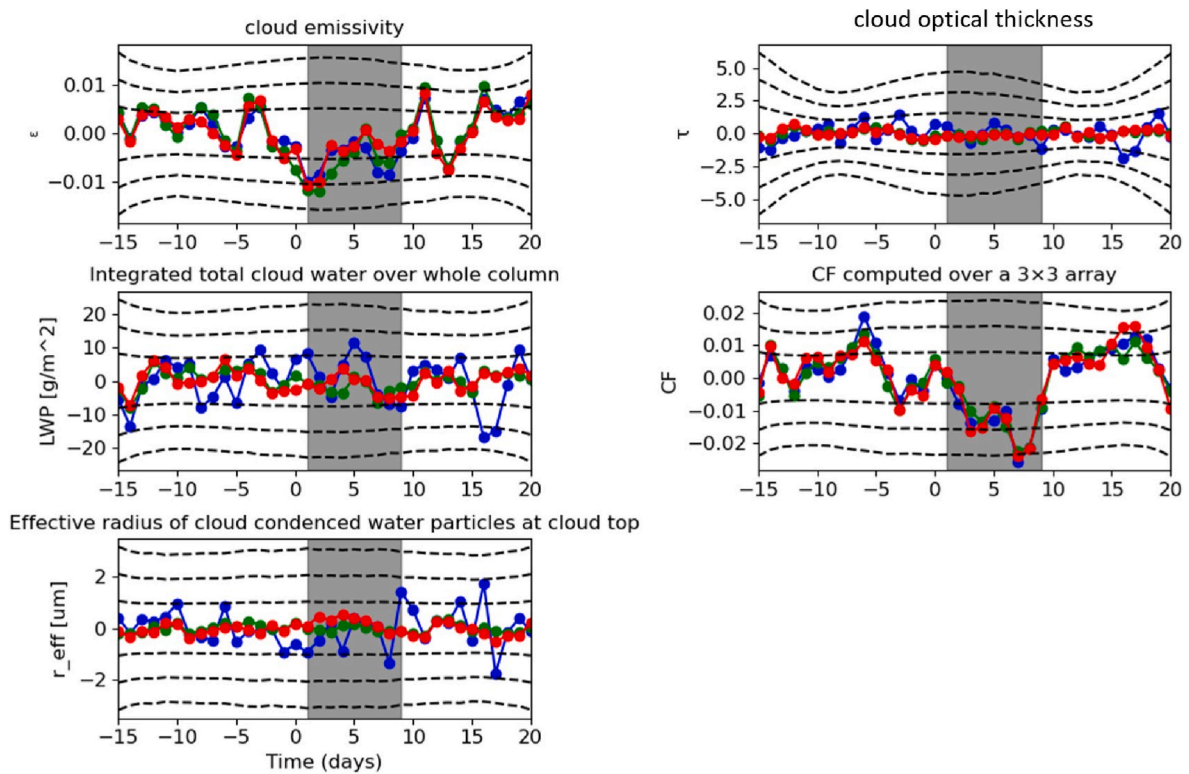


**Fig. 3.** FD rank: 1. Parameters: Cloud emissivity, integrated total cloud water over the whole column, the effective radius of cloud condensed water particles at cloud top, cloud optical depth, and cloud area fraction computed over a  $3 \times 3$  array. Satellites used: NOAA 15 (blue), 16 (green), and 17 (red). The hatched area is the integration period for the Monte Carlo analysis set between  $t_1$  and  $t_9$ . The dashed lines 1, 2, and 3  $\sigma$  are calculated by random sampling from the NOAA15 satellite data.

(ACHA) in the PATMOS-x calibration process (Heidinger and Pavolonis, 2009). In Fig. 6, the global average of the cloud emissivity from the PATMOS-x data is plotted for 36 days. We can observe a decrease in the emissivity of 0.0079 from the average value (0.68) between  $t_{-15}$  and  $t_0$  after an FD minimum (Table 7). The ASL from the Monte Carlo analysis is 0.11%. However, the cloud emissivity started decreasing around  $t_{-7}$ , as shown in Fig. 6. This is before the point depicting the minimum number of cosmic rays owing to FDs and earlier than the reaction in cloud fraction. Although cosmic ray flux also started decreasing a few days before the minimum point, the FDs' effects do not instantaneously change the characteristics of clouds. Aerosols take several days to gradually grow and activate the particle size in CCN depending on

various parameters, including the probability of cloud processing time or atmospheric material. Thus, the results of the Monte Carlo analysis between  $t_1$  and  $t_9$  indicates a highly significant signal during FDs; however, this might not reflect solely the effects of FDs, thereby exhibiting a cause-effect connection with other factors that have not yet been studied.

#### 4.2. Cloud fraction

The cloud fraction is computed over a  $3 \times 3$ -pixel (degree) resolution on the satellite cloud mask arrays at the native resolution, which are centred on the pixel from the naive Bayesian formulations (Heidinger

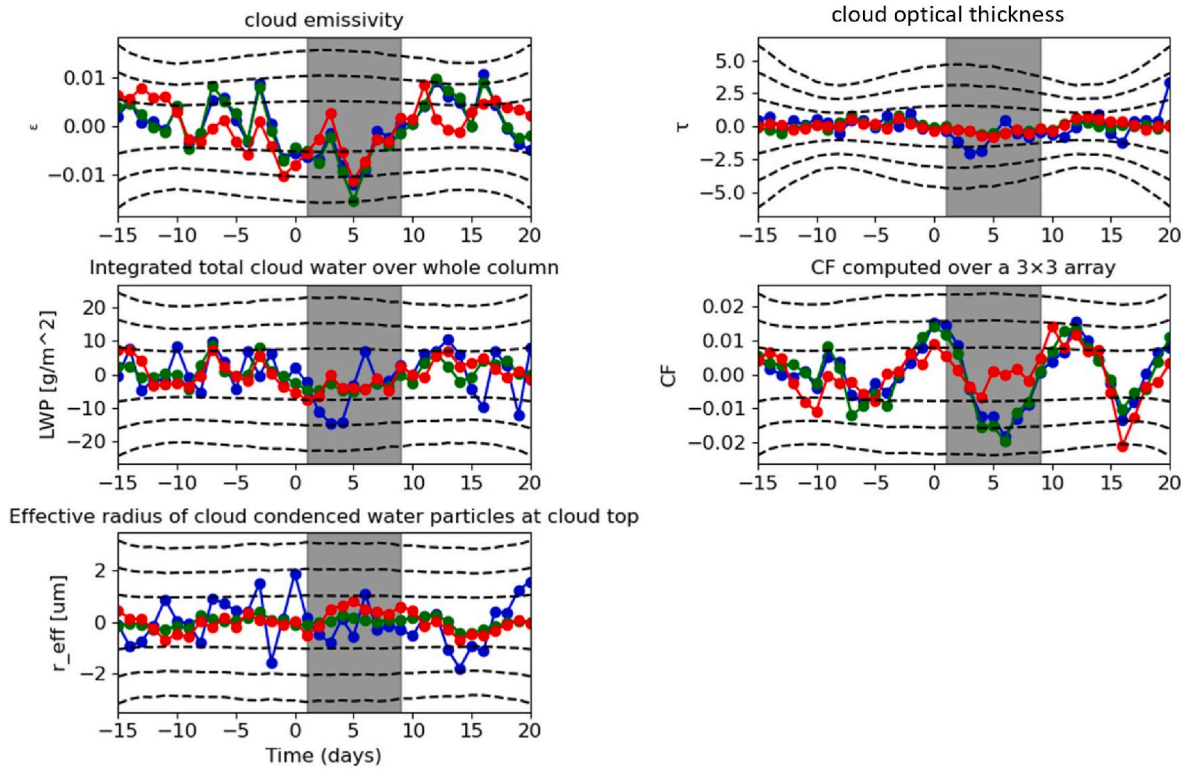


Fig. 4. FD rank: 3. Parameters: Cloud emissivity, integrated total cloud water over the whole column, effective radius of cloud condensed water particles at cloud top, cloud optical depth, and cloud area fraction computed over a  $3 \times 3$  array. Satellites used: NOAA 15 (blue), 16 (green), and 17 (red). The hatched area is the integration period for the Monte Carlo analysis set between  $t_1$  and  $t_9$ . The dashed lines 1, 2, and 3  $\sigma$  are calculated by random sampling from the NOAA15 satellite data.

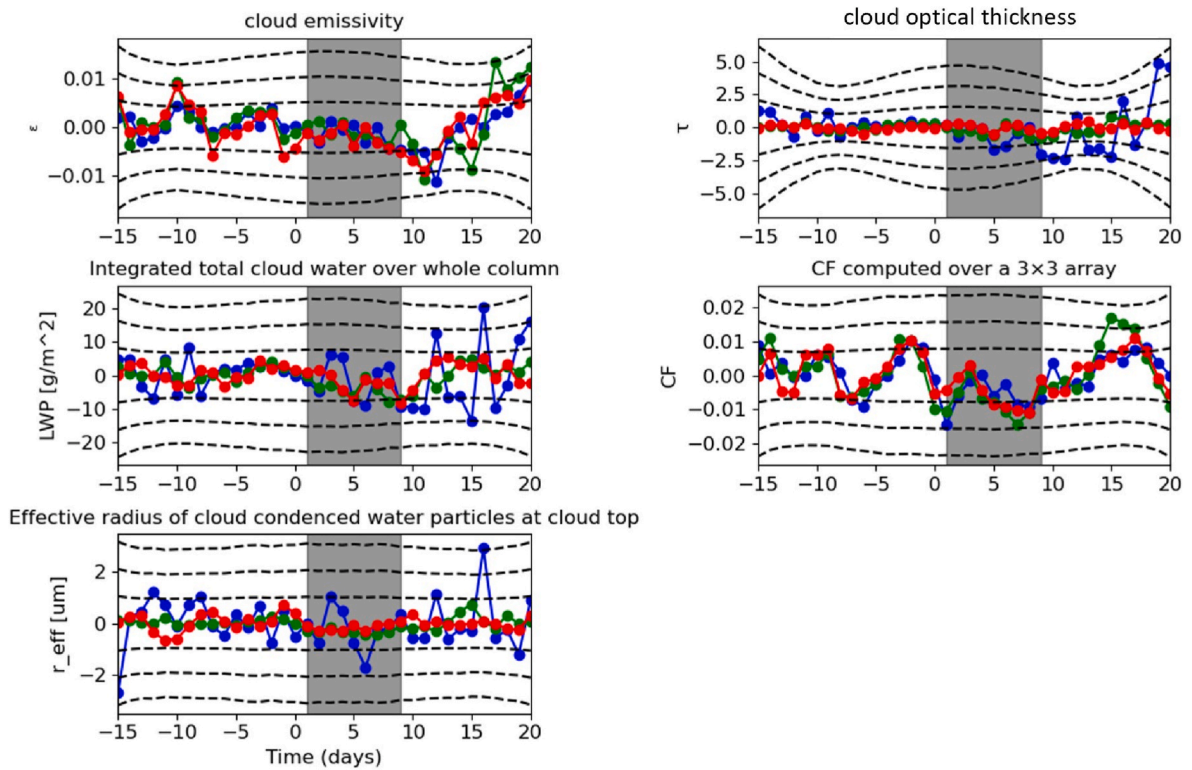
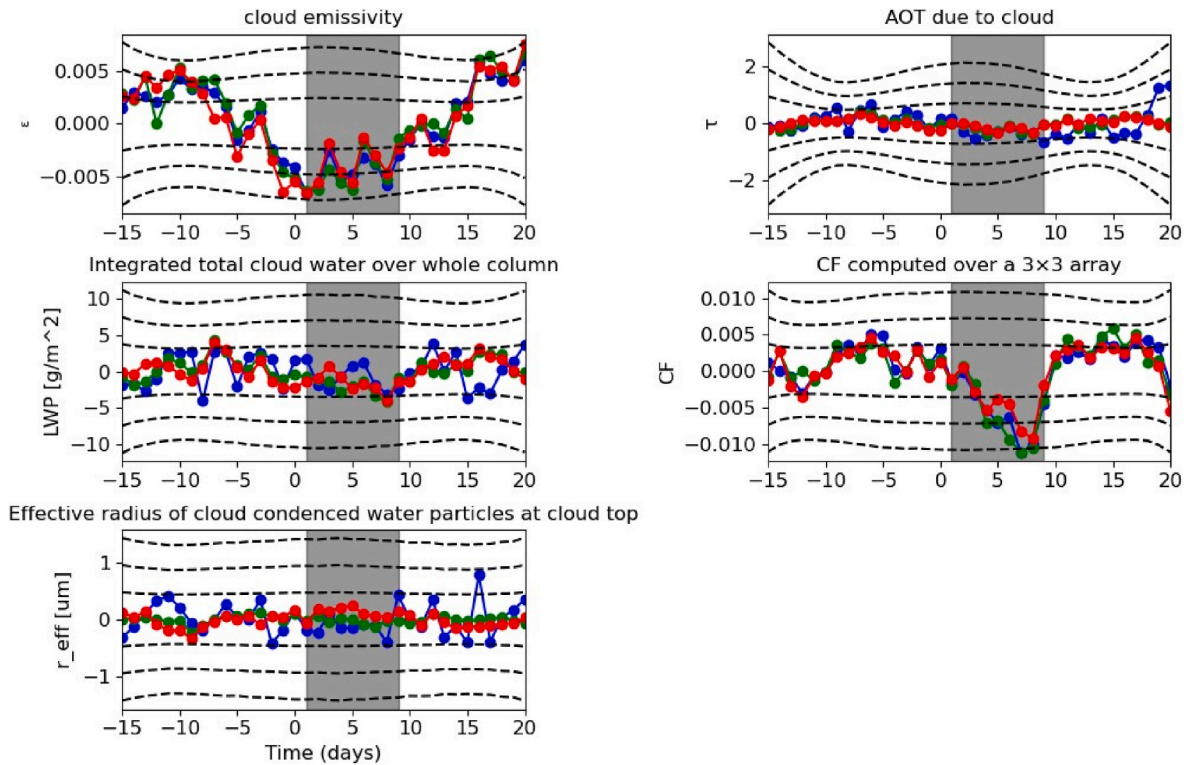


Fig. 5. FD rank: 4. Parameters: Cloud emissivity, integrated total cloud water over the whole column, the effective radius of cloud condensed water particles at cloud top, cloud optical depth, and cloud area fraction computed over a  $3 \times 3$  array. Satellites used: NOAA 15 (blue), 16 (green), and 17 (red). The hatched area is the integration period for the Monte Carlo analysis set between  $t_1$  and  $t_9$ . The dashed lines 1, 2, and 3  $\sigma$  are calculated by random sampling from the NOAA15 satellite data.



**Fig. 6.** FD rank and satellite combination:  $FD_1$  with NOAA15,  $FD_2$  with NOAA11,  $FD_3$  with NOAA15,  $FD_4$  with NOAA15,  $FD_5$  with NOAA11 (blue),  $FD_1$  with NOAA16,  $FD_2$  with NOAA11,  $FD_3$  with NOAA16,  $FD_4$  with NOAA16,  $FD_5$  with NOAA11 (green),  $FD_1$  with NOAA17,  $FD_2$  with NOAA11,  $FD_3$  with NOAA17,  $FD_4$  with NOAA17, and  $FD_5$  with NOAA11 (red). Parameters: Cloud emissivity, integrated total cloud water over the whole column, the effective radius of cloud condensed water particles at cloud top, cloud optical depth, and cloud area fraction computed over a  $3 \times 3$  array. The hatched area is the integration period for the Monte Carlo analysis set between  $t_1$  and  $t_0$ . The dashed lines 1, 2, and 3  $\sigma$  are calculated by random sampling from the NOAA15 satellite data.

**Table 4**

Monte Carlo analysis test parameters.  $t_a$  and  $t_b$  are selected to follow nucleation and growth of particles.

$N_B$	10,000
$N_{FD}$	5
$w_i$	$\frac{FD_j(\text{Strength})}{\sum_{j=1}^{N_{FD}} FD_j(\text{Strength})}$
$t_a$	1
$t_b$	9

**Table 5**

Monte Carlo analysis ASL (%) from FD rank ( $FD_1$ ,  $FD_2$ ,  $FD_3$ ,  $FD_4$ , and  $FD_5$ ) with three different satellite combinations (NOAA 15, 16, and 17). Weight type:  $\frac{FD_j(\text{strength})}{\sum_{j=1}^{N_{FD}} FD_j(\text{strength})}$

Combination of satellites	NOAA15&11	NOAA16&11	NOAA17&11
Cloud emissivity	0.11	0.01	0.45
Cloud optical thickness	26.37	32.67	37.38
Integrated total cloud water over whole column	35.65	11.44	21.23
Cloud area fraction computed over a $3 \times 3$ array	0.33	0.28	1.74
Effective radii of cloud condensed water particles at cloud top	22.79	44.4	70.78

et al., 2012). Cloud fraction denotes the proportion of the Earth's surface covered by clouds. As shown in Fig. 6, the global average cloud fraction shows a decrease in the number of clouds after an FD event with an ASL of 0.33%. The change in the cloud cover fraction caused by FDs is 0.013

**Table 6**

Monte Carlo analysis ASL (%) based on FD rank ( $FD_1$ ,  $FD_2$ ,  $FD_3$ ,  $FD_4$ , and  $FD_5$ ) derived from NOAA 15 & 11 satellites with 2 different weight types.

Statistical weight type	$\frac{FD_j(\text{strength})}{\sum_{j=1}^{N_{FD}} FD_j(\text{strength})}$	$\frac{1}{N_{FD}}$ for $i = [1, 2, \dots, N_{FD}]$
Cloud emissivity	0.11	0.15
Cloud optical thickness	26.37	23.55
Integrated total cloud water over whole column	35.65	30.14
Cloud area fraction computed over a $3 \times 3$ array	0.33	0.81
Effective radii of cloud condensed water particles at cloud top	22.79	25.78

**Table 7**

Mean  $\pm \sigma$  is the mean value of the superposed five FD events from  $t_{-16}$  to  $t_0$ . Signal (%) is the maximum value during  $t_1$  and  $t_0$  compared with the mean from  $t_{-16}$  to  $t_0$ . Noise (%) is the Monte Carlo analysis-based one-sigma standard deviation on the day that the highest signal occurs, compared with the mean from  $t_{-16}$  to  $t_0$ .

	Mean $\pm \sigma$	Signal (%)	Noise (%)
Cloud emissivity [-]	0.68 $\pm$ 0.0052	1.16	0.77
COT [-]	14.61 $\pm$ 1.28	0.85	8.79
LWP [ $g/m^2$ ]	140.21 $\pm$ 5.87	3.1	4.18
CF [-]	0.66 $\pm$ 0.0035	2.3	0.53
$r_{eff}$ [ $\mu m$ ]	21.47 $\pm$ 1.0064	1.1	4.6
TABT (3.75 $\mu m$ ) [K]	279.87 $\pm$ 0.56	0.048	0.2
TABT (11 $\mu m$ ) [K]	271.95 $\pm$ 0.72	0.062	0.26
TABT (12 $\mu m$ ) [K]	270.69 $\pm$ 0.72	0.064	0.27
Surface brightness temperature [K]	275.26 $\pm$ 0.75	0.093	0.27

from the peak to the average levels for days  $-15$  to  $0$ , as shown in Fig. 6. This corresponds to 2.3% of the global average cloud fractions (0.66). Cloud probability is derived from radiance and reflectance measurements performed by the AVRHH using a naive Bayesian approach (Heidinger et al., 2012). The details of the classical Bayesian approach are explained in Uddstrom et al. (1999) and Merchant et al. (2005). The naive Bayesian formulation allows for multiple cloud classifiers to be used without the need for large arrays.

#### 4.3. Cloud optical depth, effective radius of cloud condensed water particles, and integrated total cloud water over whole column

COT from PATMOS-x represents the vertical optical depth between the top and bottom of an atmospheric column for both liquid and ice cloud. Additionally,  $r_{eff}$  is defined by the ratios of the integral over all droplet volumes to the integral over all droplet surface areas. COT is pivotal for understanding cloud radiative forcing, effective radius distributions, and LWP. Here, COT,  $r_{eff}$ , and LWP did not show a strong significant response to FDs, as shown in Fig. 6. In other studies, the Angstrom exponent for the wavelengths 340–440 nm from AERONET, liquid cloud optical thickness, and liquid cloud effective radius from MODIS showed a significant response to the FD events when using the same Monte Carlo statistical method (Svensmark et al., 2016). In Table 7, each parameter's signal and noise are noted. As compared to the signal size determined by Svensmark et al. (2016), the signal size from PATMOS-x is smaller than the noise (e.g. signal level of COT from PATMOS-x and MODIS are 0.13 and approximately 0.1 each, and noise level from PATMOS-x and MODIS are 1.28 and 0.06 each); thus, it is difficult to confirm whether there is a signal because the noise level of PATMOS-x is adequately large to hide the signal. In the research by Svensmark et al. (2016), MODIS data did not cover the dates (June 13, 1991) and (March 15, 1989), which showed the second and fifth strongest FD events; this helped create different results from the Monte Carlo analysis between PATMOS-x and MODIS. COT,  $r_{eff}$ , and LWP are

estimated using the daytime cloud optical and microphysical properties (DCOMP) algorithm (Walther and Heidinger, 2012). When COT and  $r_{eff}$  are obtained using same channel observations, LWP can be derived from them. This implies that these three parameters are connected during retrieval. For example, LWP measurements depend on COT and  $r_{eff}$  data quality; as such, any noise or errors from the COT and  $r_{eff}$  retrievals propagates to the LWP determination. In general, the CCN product is difficult to retrieve without some noise over land (Levy et al., 2010). Therefore, satellite observation is more sensitive to uncertainties when compared with COT measurements obtained from ground-based observatories (Rawlins and Foot, 1990). When we investigate the difference between PATMOS-x and MODIS, these satellites use the same DCOMP algorithm to retrieve the parameters. However, discrepancies are found when DCOMP on MYD06 (derived from MODIS) and on AVHRR (derived from PATMOS-x) are compared with values of  $r_{eff}$  because of the different cloud sampling methods (Walther and Heidinger, 2012). Nevertheless, differences between PATMOS-x and MODIS products do not necessarily imply a low quality of DCOMP products; rather, they reveal the results of different retrieval approaches that use varying ancillary data, such as the surface albedo.

#### 4.4. Brightness temperature

BT is a unique form of temperature; it is the apparent temperatures retrieved using radiance measurements via the inversion of Planck's law, while assuming a surface emissivity of 1.0. If the emissivity is lower than 1.0, the radiance emitted by the cloud does not exactly correspond to the radiance from a black body at the same temperature. The AVRHH uses measurements at wavelengths of 3.75, 11, and 12  $\mu\text{m}$  for determining surface BTs (Heidinger et al., 2014). The PATMOS-x data show a response to FD (6.37%, 3.66%, and 6.71%) for the global average of TABTs at wavelengths of 3.75, 11.0, and 12.0  $\mu\text{m}$  (Fig. 7); the TABTs increased by 0.24, 0.17, and 0.14 K. The surface BTs based on the measurement parameters in Fig. 7 show an increase in temperature

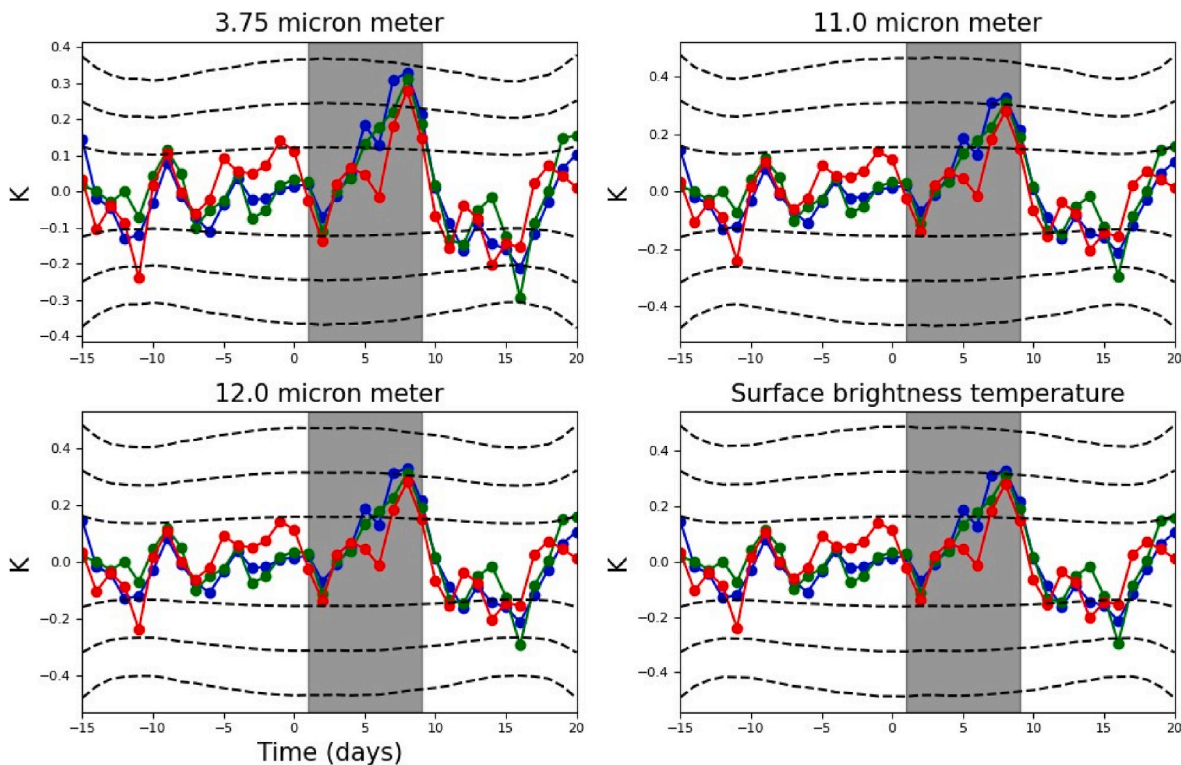


Fig. 7. TABT at the nominal wavelengths of 3.75, 11.0, and 12.0  $\mu\text{m}$ , and surface BT [K]. Superposed FDs: five strongest events; satellites used: NOAA11 and each 15 (blue), 16 (green), and 17 (red). The dashed lines 1, 2, and 3  $\sigma$  are calculated by random sampling from the NOAA15 satellite.

following FDs at a 4.48% significance level with an increase of 0.28 K.

### 5. Discussion

In this study, we showed a significant decrease in cloud cover fraction and emissivity; a weak change in COT,  $r_{eff}$ , and LWP; and an increase in BT during FDs. The observed changes in cloud physics may explain the behaviour of the BT. The top of the atmosphere cloud radiance is affected by various factors such as surface albedo, cloud thickness, aerosol optical depth, and particle size (Liao and Seinfeld, 1998). To analyse this, we used the Fu-Liou radiative transfer model (Fu and Liou, 1993), which uses the  $\delta$ -four-stream approximation for calculating the transfer of radiative fluxes in the atmosphere for a single homogeneous layer integrated over six SW bands (0.2–0.7, 0.7–1.3, 1.3–1.9, 1.9–2.5, 2.5–3.5, and 3.5–4.0  $\mu\text{m}$ ) and 12 LW bands (2200–1900, 1900–1700, 1700–1400, 1400–1250, 1250–1100, 1100–980, 980–800, 800–670, 670–540, 540–400, 400–280, and 280–0  $\text{cm}^{-1}$ ) (Liou et al., 1988; Fu and Liou, 1993). We used a 36-day time series for cloud emissivity, cloud fraction, COT,  $r_{eff}$ , and LWP during the five strongest FDs as input to simulate SW and LW radiation changes. The results are shown in Fig. 9. The maximum change in SW radiation during FDs ( $3.69 \text{ W/m}^2$ ) is larger than the maximum change in LW radiation ( $0.36 \text{ W/m}^2$ ) for a pressure range from 680 to 955 hPa. The net result of the increased incoming radiation is thus  $3.33 \text{ W/m}^2$ . Note that the amount of solar radiative energy incident also changes quickly during FD since the cloud coverage change during FD events alters the surface albedo as well, which is comparable in magnitude to what happens during the 11-year solar cycle that changes the amount of solar

radiative energy incident on Earth by  $\pm 0.1\%$ . The maximum to minimum peak amplitude of these variations is approximately  $0.25 \text{ W/m}^2$  at the ground level ( $0.1\%$  of  $1367/4 \times 0.7 \text{ W/m}^2$ , assuming a TSI of  $1367 \text{ W/m}^2$  at 1 AU and an albedo of 0.3).

This is not enough to cause even a 0.1 K change in the Earth's equivalent black body temperature (Feulner and Rahmstorf, 2010; Jones et al., 2012; Anet et al., 2013).

The cosine solar zenith angle is set to a constant 0.5 in this model, since cosine zenith angles of 0.5 is used as the daytime average. However, the input data from PATMOS-x is a mix of several events and calculated based on a global average. Thus, based on this model, this will create an error in any radiation change estimation. The radiative fluxes are influenced by variations in cloud fraction and cloud optical depth. The Fu-Liou model calculates the top of the atmosphere radiative forcing from multiple cloud layers, with each cloud fraction in a cloud overlap assumption (Jakob and Klein, 1999). Cloud fraction represents each subgrid box; for example, a radiation variance is only treated by a change in cloud fraction in global circulation models with numerical weather prediction (Jakob and Klein, 1999). In other studies, cloud fraction is considered a sensitive parameter affecting atmospheric radiative rates by the Fu-Liou-Gu plane-parallel radiation model (Liu et al., 2017). Surface solar radiation measurements by pyranometers are especially sensitive to the cloud amount at low and moderate levels, while cloud type governs the surface solar radiation (Harrison et al., 2008). Thus, the radiation change may be explained by cloud fraction.

We also calculated changes in the BT of the skin temperature of oceans using Eq. (18). The penetration depth from the surface is set to 1 mm because the satellite can measure the temperature of the skin layer

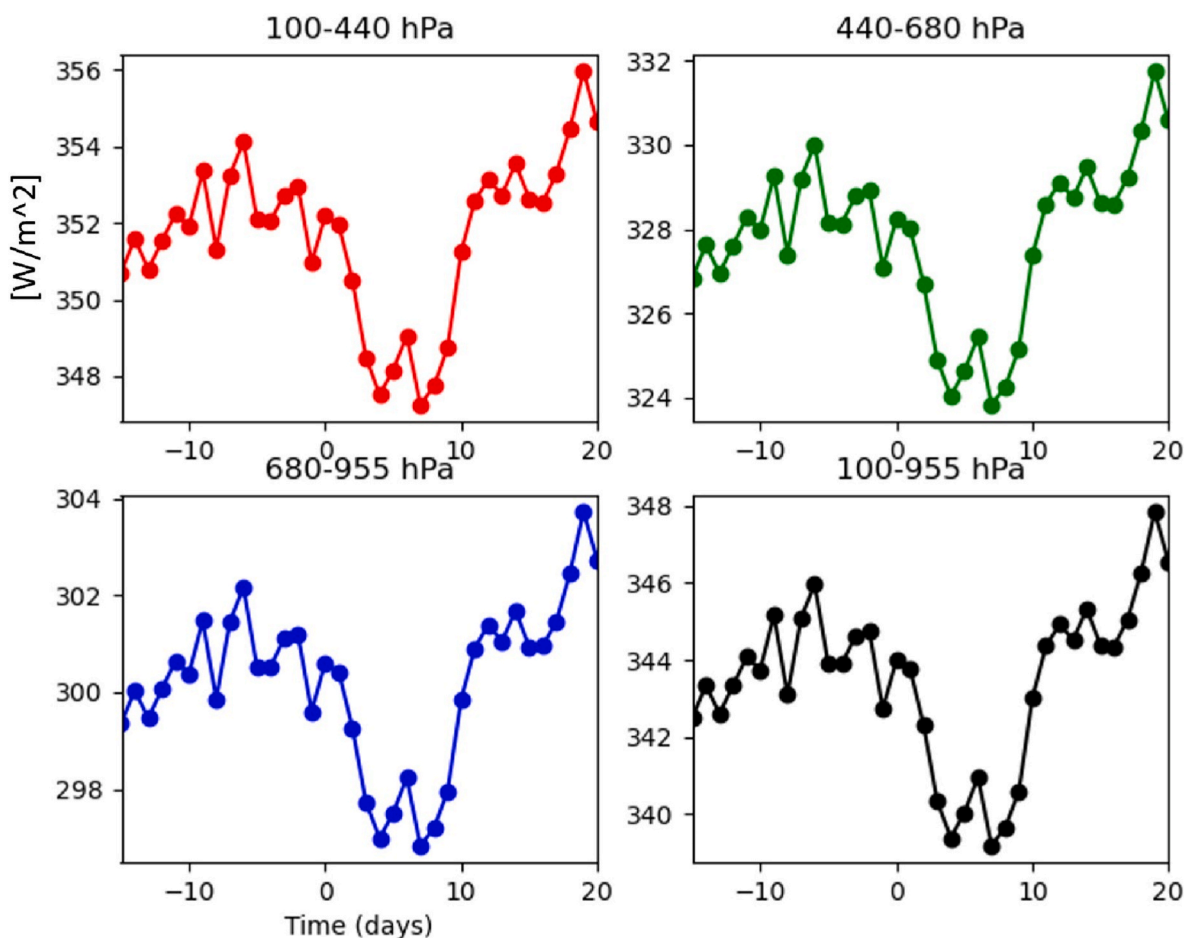


Fig. 8. Outgoing SW radiation according to the Fu-Liou model. The pressure at the top of the cloud is between 100 and 955 hPa. Cloud phase: water. Cosine solar zenith angle: 0.5.

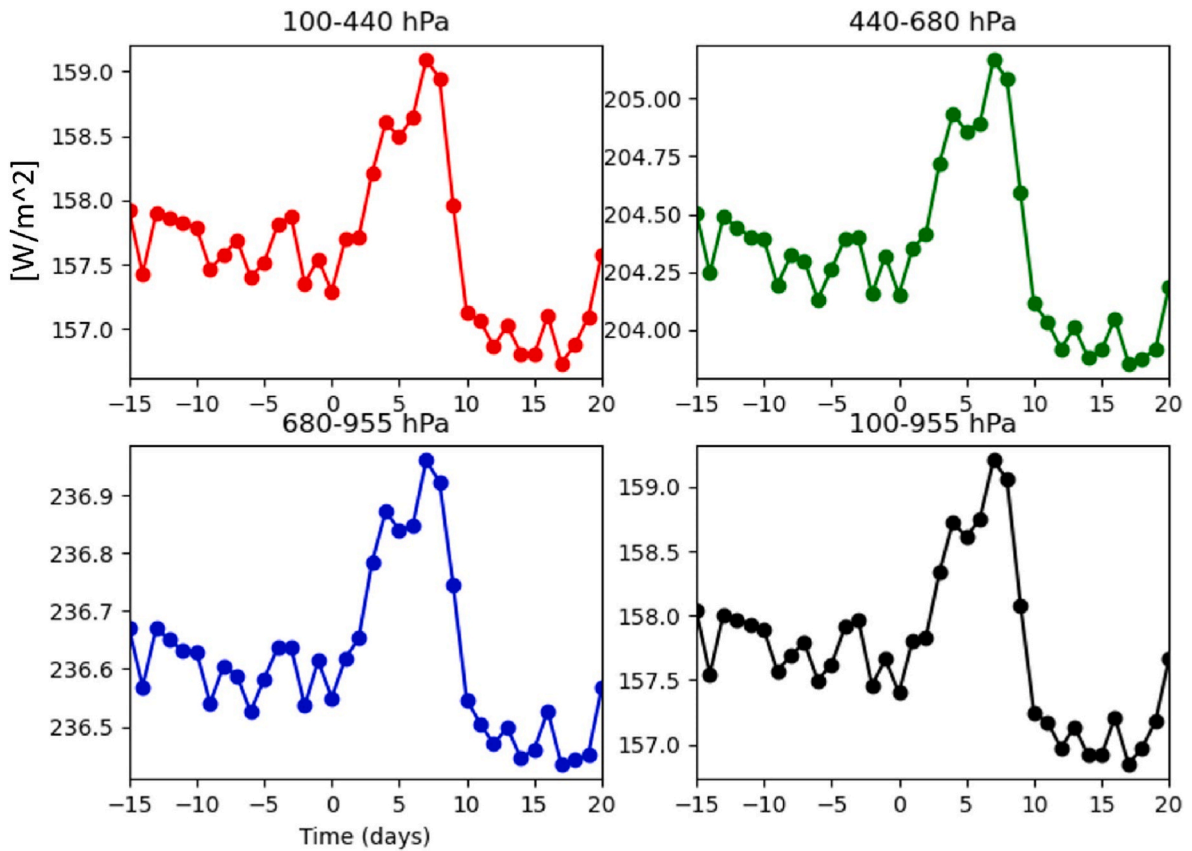


Fig. 9. Outgoing LW radiation according to the Fu-Liou model. The pressure at the top of the cloud is between 100 and 955 hPa. Cloud phase: water. Cosine solar zenith angle: 0.5.

of the ocean surface that is less than 1 mm deep (Talley, 2011). The forcing output from the Fu-Liou model at a resolution of 1 day was linearly interpolated to a 1 s timescale and used as input for the calculation, which requires a small-time step. The output results show a

response of 0.61 K, which is higher than the observation results shown in Fig. 7. However, this indicates that the surface temperature at a depth of 1 mm can respond quickly to the changed cloud forcing, as seen in Figs. 8, 9 and 10. Note that the BT data from the PATMOS-x represents a

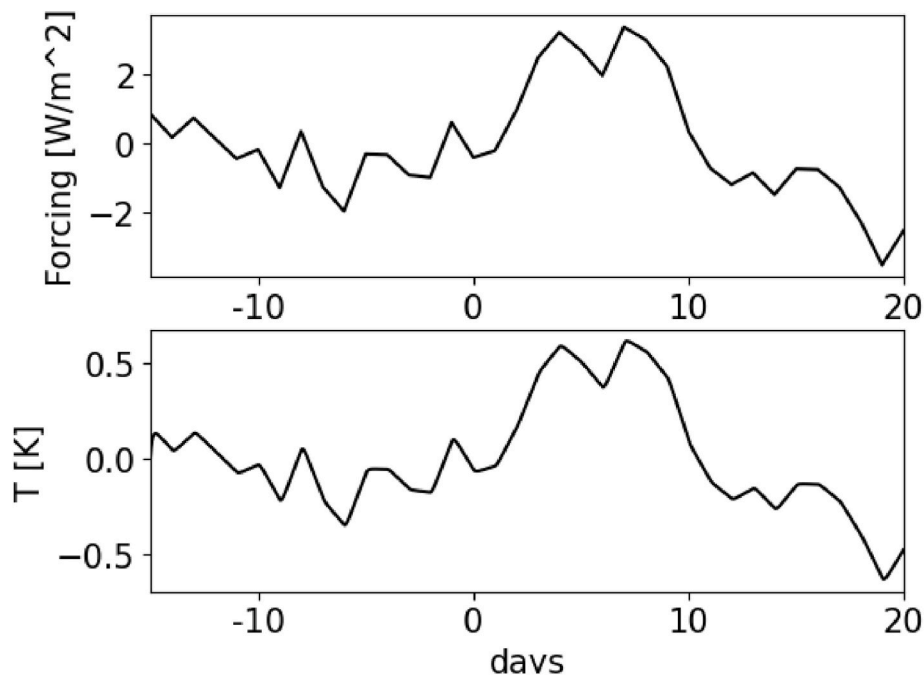


Fig. 10. Top: Forcing change from the Fu-Liou model. Bottom: Calculated brightness temperature at the surface of an ocean for comparison with model and measurements.

combination of land and ocean areas that have different heat capacities, which may explain why the calculation and observation differ slightly. Another possible explanation is that a decrease in cloud top height can explain the increase in BT during FDs. Therefore, we analysed the cloud top height from the PATMOS-x data during FDs. However, it did not exhibit any significant signal.

$$C\rho l \frac{dT_{oce}(t)}{dt} = F(t) - \lambda T_{oce}(t) \quad (17)$$

$$T_{oce}(t) = \int_{-\infty}^t e^{-\frac{\lambda(t-t')}{C\rho l}} \frac{F(t')}{C\rho l} dt' \quad (18)$$

where  $T_{oce}$  is the BT at the surface of an ocean;  $\lambda$  represents the heat loss in the ocean skin ( $5.42 \text{ W/m}^2\text{K}$ ), which is derived from the expansion of  $\sigma T^4$  when Earth's surface temperature is assumed to be  $288 \text{ K}$ ;  $C$  denotes the heat capacity of water ( $4.2 \times 10^3 \text{ J/kgK}$ );  $\rho$  is the density of water ( $1.0 \times 10^3 \text{ kg/m}^3$ );  $l$  is the thickness of the skin layer ( $1.0 \times 10^{-3} \text{ m}$ ); and  $F$  is the forcing variation estimated from the Fu-Liou model.

## 6. Conclusion

In this study, the newly calibrated PATMOS-x data set from 1978 to 2018 was analysed to study the effect of FD on the atmosphere. The five strongest FD events were selected based on their percentage decrease in ion production. This is because GCR arriving in the atmosphere produces ions, and promotes the nucleation process of particles (Wagner et al., 2017; Kirkby et al., 2016; Tomicic et al., 2018; Lehtipalo et al., 2016). We examined the significance level of the FD effects on ten parameters, including some that were previously unexplored, namely: TABT at the nominal wavelengths of 3.75, 11.0, and  $12.0 \mu\text{m}$  and surface BT with high ASL levels (ASL 6.71%, 3.66%, 6.37%, and 4.48%). A radiative model (Fu-Liou model) was used to estimate the LW and SW radiation resulting from the detected changes in cloud parameters. This calculated forcing effect during FDs is sufficient to change the Earth's surface temperature, with the penetration depth being detectable by a satellite (1 mm) for a short period (i.e., a few days); this result agrees well with the detected signal in BT. The effects of FDs shown in this analysis were consistent with the results from other studies on cloud fraction (ASL 0.33%) (Svensmark et al., 2016). These results also support other studies; for example, those of H. Svensmark et al. (2009) and Pudovkin and Veretenenko (1995). Cloud emissivity seemingly showed signals with the proposed method, but did not respond simultaneously with cloud fractions. Cloud emissivity started to change several days before  $t_0$ , and this instant change cannot be explained by the aerosol's growth process, cloud lifetime, and other changes in cloud features. Thus, cloud emissivity does not show any physical effect of FDs; however, it does reveal other factors that have not been investigated yet. Overall, this response was random and had a low occurrence chance, which implies that it is a product of the method or a spurious signal. Signals of OT, LWP, and  $r_{eff}$  associated with cloud water particles were not strongly significant, with an ASL of 26.37, 35.65, and 22.79%, respectively. This is more likely caused by a larger noise level of the data sets, the difference in retrieval processes, and different combinations of the five strongest FD events as compared to those of previous studies.

Moreover, the ion-induced nucleation process creates particles of size less than  $0.1 \mu\text{m}$ ; thus, any aerosols produced with the assistance of ions must grow considerably to be detectable by satellites, which use detection wavelengths of approximately 500 nm. Of course, scattering theory should be considered to estimate the available particle sizes via observation. Nevertheless, these results will be useful to better understand cloud microphysical structures under various atmospheric conditions and will provide a better understanding of the Earth's climate and weather changes occurring due to cosmic rays and solar activities. In future work, other calibrated satellites or observational data should be

utilised for determining new aspects beyond the scope of this study, such as the consideration of geological factors (e.g. land type, latitudinal area, or seasonal effects). In conclusion, among the several analysed atmospheric/cloud/aerosol parameters, cloud fraction and TABT at nominal wavelengths of 3.75, 11.0, and  $12.0 \mu\text{m}$  are the only parameters depicting a statistically significant and correct-phase response to FDs.

## Declaration of competing interest

The authors declare that they have no known competing financial interests or personal relationships that could have appeared to influence the work reported in this paper.

## Acknowledgments

PATMOS-x data used for Monte Carlo analysis in this research can be downloaded from the website <https://cimss.ssec.wisc.edu/patmosx/>. This work was performed using the Fu-Liou radiative transfer model, which is available from the website <https://web.archive.org/web/20100527145310/http://snowdog.larc.nasa.gov/cgi-bin/rose/flp200503/flp200503.cgi>. The authors wish to thank Jacob Svensmark for his advice and comments on our research as well as the two reviewers for their suggestions for improving the statistical method and data handling.

## Acronyms

<b>FDs</b>	Forbush decreases
<b>CCN</b>	Cloud condensation nuclei
$r_{eff}$	Cloud effective radius
<b>PATMOS-x</b>	Pathfinder Atmospheres Extended
<b>AVHRR</b>	Advanced very high resolution radiometer
<b>ASLs</b>	Achieved Significance Levels
<b>LWP</b>	Integrated total cloud water over the whole column
<b>CME</b>	Coronal mass ejection
<b>GCRs</b>	Galactic cosmic rays
<b>ISCCP</b>	International Satellite Cloud Climatology Project
<b>TSI</b>	Total solar irradiance
<b>CLOUD</b>	Cosmics Leaving Outdoor Droplets
<b>SSM/I</b>	Special Sensor Microwave/Imager
<b>MODIS</b>	Moderate resolution imaging spectroradiometer
<b>AERONET</b>	Aerosol robotic network
<b>LCF</b>	Liquid water cloud fraction
<b>CI</b>	Cloud index
<b>Occ</b>	Cloud occurrence frequency
<b>Ext</b>	Extinction data
<b>CNM</b>	Climax neutron monitor data
<b>DTR</b>	Diurnal temperature range
<b>NOAA</b>	National Oceanic and Atmospheric Administration
<b>POES</b>	Polar Operational Environmental Satellites
<b>GOES</b>	Geostationary Operational Environmental Satellite
<b>EUMESAT</b>	Exploitation of meteorological satellites
<b>METOP</b>	Meteorological Operational Satellite
<b>COT</b>	Cloud optical thickness (atmosphere optical depth due to the cloud)
<b>TABT</b>	Top of the atmosphere brightness temperature
<b>WDCCR</b>	World Data Centre for Cosmic Rays
<b>LW</b>	Long-wave
<b>ACHA</b>	AWG Cloud Height Algorithm
<b>DCOMP</b>	Daytime cloud optical and microphysical properties
<b>BT</b>	Brightness temperature
<b>GCM</b>	Global circulation model

## References

- Anet, J.G., Rozanov, E., Muthers, S., Peter, T., Brönnimann, S., Arfeuille, F., et al., 2013. Impact of a potential 21st century “grand solar minimum” on surface temperatures and stratospheric ozone. *Geophys. Res. Lett.* 40 (16), 4420–4425.
- Calogovic, J., Albert, C., Arnold, F., Beer, J., Desorgher, L., Flueckiger, E., 2010. Sudden cosmic ray decreases: No change of global cloud cover. *Geophys. Res. Lett.* 37 (3).
- Dragic, A., Anicin, I., Banjanac, R., Udovčić, V., Joković, D., Maletić, D., Puzović, J., 2011. Forbush decreases—clouds relation in the neutron monitor era. *Astrophys. Space Sci. Trans.* 7 (3), 315–318.
- Efron, B., Tibshirani, R.J., 1994. *An Introduction to the Bootstrap*. CRC press.
- Feulner, G., Rahmstorf, S., 2010. On the effect of a new grand minimum of solar activity on the future climate on earth. *Geophys. Res. Lett.* 37 (5).
- Forbush, S., 1937. A model for particle formation and growth in the atmosphere with molecular resolution in size. *Phys. Rev.* 51, 1108.
- Fu, Q., Liou, K.N., 1993. Parameterization of the radiative properties of cirrus clouds. *J. Atmos. Sci.* 50 (13), 2008–2025.
- Garrett, T.J., Radke, L.F., Hobbs, P.V., 2002. Aerosol effects on cloud emissivity and surface longwave heating in the arctic. *J. Atmos. Sci.* 59 (3), 769–778.
- Harrison, R.G., Chalmers, N., Hogan, R.J., 2008. Retrospective cloud determinations from surface solar radiation measurements. *Atmos. Res.* 90 (1), 54–62.
- Heidinger, A.K., Evan, A.T., Foster, M.J., Walther, A., 2012. June. A naive bayesian cloud-detection scheme derived from CALIPSO and applied within PATMOS-x. *J. Appl. Meteorol. Climatol.* 51 (6), 1129–1144. <https://doi.org/10.1175/jamc-d-11-02.1>. Retrieved from <https://doi.org/10.1175/jamc-d-11-02.1>.
- Heidinger, A.K., Foster, M.J., Walther, A., Zhao, X., 2014. The pathfinder atmospheres—extended avhrr climate dataset. *Bull. Am. Meteorol. Soc.* 95 (6), 909–922.
- Heidinger, A.K., Pavlonis, M.J., 2009. Gazing at cirrus clouds for 25 years through a split window. part i: Methodology. *J. Appl. Meteorol. Climatol.* 48 (6), 1100–1116.
- Jakob, C., Klein, S.A., 1999. The role of vertically varying cloud fraction in the parameterization of microphysical processes in the ecmwf model. *Q. J. R. Meteorol. Soc.* 125 (555), 941–965.
- Jones, G.S., Lockwood, M., Stott, P.A., 2012. What influence will future solar activity changes over the 21st century have on projected global near-surface temperature changes. *J. Geophys. Res. Atmos.* 117 (D5).
- Kirkby, J., Curtius, J., Almeida, J., Dunne, E., Duplissy, J., Ehrhart, S., et al., 2011. Role of sulphuric acid, ammonia and galactic cosmic rays in atmospheric aerosol nucleation. *Nature* 476 (7361), 429.
- Kirkby, J., Duplissy, J., Sengupta, K., Frege, C., Gordon, H., Williamson, C., et al., 2016. Ion-induced nucleation of pure biogenic particles. *Nature* 533 (7604), 521–526.
- Kristjánsson, J.E., Kristiansen, J., 2000. Is there a cosmic ray signal in recent variations in global cloudiness and cloud radiative forcing? *J. Geophys. Res. Atmos.* 105 (D9), 11851–11863.
- Kulmala, M., Vehkamäki, H., Petäjä, T., Maso, M.D., Lauri, A., Kerminen, V.-M., et al., 2004. March. Formation and growth rates of ultrafine atmospheric particles: a review of observations. *J. Aerosol Sci.* 35 (2), 143–176. <https://doi.org/10.1016/j.jaerosci.2003.10.003>. Retrieved from <https://doi.org/10.1016/j.jaerosci.2003.10.003>.
- Laken, B., Wolfendale, A., Kniveton, D., 2009. Cosmic ray decreases and changes in the liquid water cloud fraction over the oceans. *Geophys. Res. Lett.* 36 (23).
- Laken, B.A., Calogović, J., 2011. Solar irradiance, cosmic rays and cloudiness over daily timescales. *Geophys. Res. Lett.* 38 (24).
- Lehtipalo, K., Rondo, L., Kontkanen, J., Schobesberger, S., Jokinen, T., Sarnela, N., et al., 2016. The effect of acid-base clustering and ions on the growth of atmospheric nanoparticles. *Nat. Commun.* 7 (1), 1–9.
- Levy, R., Remer, L., Kleidman, R., Mattoo, S., Ichoku, C., Kahn, R., Eck, T., 2010. Global evaluation of the collection 5 modis dark-target aerosol products over land. *Atmos. Chem. Phys.* 10 (21), 10399.
- Liao, H., Seinfeld, J.H., 1998. Effect of clouds on direct aerosol radiative forcing of climate. *J. Geophys. Res. Atmos.* 103 (D4), 3781–3788.
- Liou, K.-N., Fu, Q., Ackerman, T.P., 1988. A simple formulation of the delta-four-stream approximation for radiative transfer parameterizations. *J. Atmos. Sci.* 45 (13), 1940–1948.
- Liu, R., Liou, K.-N., Su, H., Gu, Y., Zhao, B., Jiang, J.H., Liu, S.C., 2017. High cloud variations with surface temperature from 2002 to 2015: contributions to atmospheric radiative cooling rate and precipitation changes. *J. Geophys. Res. Atmos.* 122 (10), 5457–5471.
- Marsh, N., Svensmark, H., 2000. Cosmic rays, clouds, and climate. *Space Sci. Rev.* 94 (1–2), 215–230.
- Merchant, C., Harris, A., Maturi, E., MacCallum, S., 2005. Probabilistic physically based cloud screening of satellite infrared imagery for operational sea surface temperature retrieval. *Q. J. R. Meteorol. Soc.* 131 (611), 2735–2755.
- Nicoll, K., Harrison, R., 2010. Experimental determination of layer cloud edge charging from cosmic ray ionisation. *Geophys. Res. Lett.* 37 (13).
- Pudovkin, M., Veretenenko, S., 1995. Cloudiness decreases associated with forbush-decreases of galactic cosmic rays. *J. Atmos. Terr. Phys.* 57 (11), 1349–1355.
- Rawlins, F., Foot, J., 1990. Remotely sensed measurements of stratocumulus properties during fire using the c130 aircraft multi-channel radiometer. *J. Atmos. Sci.* 47 (21), 2488–2504.
- Rohs, S., Spang, R., Rohrer, F., Schiller, C., Vos, H., 2010. JUL 31. A correlation study of high-altitude and midaltitude clouds and galactic cosmic rays by MIPAS-Envisat [Article]. *J. Geophys. Res. Atmos.* 115 <https://doi.org/10.1029/2009JD012608>.
- Sun, B., Bradley, R.S., 2002. Solar influences on cosmic rays and cloud formation: a reassessment. *J. Geophys. Res. Atmos.* 107 (D14), AAC-5.
- Svensmark, H., Bondo, T., Svensmark, J., 2009. Cosmic ray decreases affect atmospheric aerosols and clouds. *Geophys. Res. Lett.* 36 (15).
- Svensmark, H., Enghoff, M., Shaviv, N., Svensmark, J., 2017. Increased ionization supports growth of aerosols into cloud condensation nuclei. *Nat. Commun.* 8 (1), 2199.
- Svensmark, H., Enghoff, M.B., Pedersen, J.O.P., 2013. Response of cloud condensation nuclei (<math>\zeta</math> 50 nm) to changes in ion-nucleation. *Phys. Lett.* 377 (37), 2343–2347.
- Svensmark, H., Pedersen, J.O.P., Marsh, N.D., Enghoff, M.B., Uggerhøj, U.I., 2006. Experimental evidence for the role of ions in particle nucleation under atmospheric conditions. In: *Proceedings of the Royal Society A: Mathematical, Physical and Engineering Sciences*, vol. 463, pp. 385–396 (2078).
- Svensmark, H., Svensmark, J., Enghoff, M., Shaviv, N., 2021. Atmospheric Ionization and Cloud Radiative Forcing. *Scientific Reports*(19668).
- Svensmark, J., Enghoff, M., Shaviv, N., Svensmark, H., 2016. The response of clouds and aerosols to cosmic ray decreases. *J. Geophys. Res.: Space Physics* 121 (9), 8152–8181.
- Talley, L.D., 2011. *Descriptive Physical Oceanography: an Introduction*. Academic press.
- Tinsley, B.A., 2000. Influence of solar wind on the global electric circuit, and inferred effects on cloud microphysics, temperature, and dynamics in the troposphere. *Space Sci. Rev.* 94 (1), 231–258.
- Tinsley, B.A., Deen, G.W., 1991. Apparent tropospheric response to mevgev particle flux variations: a connection via electrofreezing of supercooled water in high-level clouds? *J. Geophys. Res. Atmos.* 96 (D12), 22283–22296.
- Tinsley, B.A., Heelis, R.A., 1993. Correlations of atmospheric dynamics with solar activity evidence for a connection via the solar wind, atmospheric electricity, and cloud microphysics. *J. Geophys. Res. Atmos.* 98 (D6), 10375–10384.
- Todd, M.C., Kniveton, D.R., 2001. Changes in cloud cover associated with forbush decreases of galactic cosmic rays. *J. Geophys. Res. Atmos.* 106 (D23), 32031–32041. <https://doi.org/10.1029/2001JD000405>. Retrieved from <https://doi.org/10.1029/2001JD000405>.
- Todd, M.C., Kniveton, D.R., 2004. Short-term variability in satellite-derived cloud cover and galactic cosmic rays: an update. *J. Atmos. Terr. Phys.* 66, 1205–1211.
- Tomicic, M., Bødker Enghoff, M., Svensmark, H., 2018. Experimental study of h 2 so 4 aerosol nucleation at high ionization levels. *Atmos. Chem. Phys.* 18 (8), 5921–5930.
- Tsubota, Y., 1995. *Analysis of the Effect of Solar Irradiance Variability on Global Sea Surface Temperature and Climate: An Investigation Using The Nasa, Goddard Institute for Space Studies General Circulation Model* (Unpublished Doctoral Dissertation). Columbia University, New York, N.Y.
- Uddstrom, M.J., Gray, W.R., Murphy, R., Oien, N.A., Murray, T., 1999. A bayesian cloud mask for sea surface temperature retrieval. *J. Atmos. Ocean. Technol.* 16 (1), 117–132.
- Udelhofen, P.M., Cess, R.D., 2001. Cloud cover variations over the United States: an influence of cosmic rays or solar variability? *Geophys. Res. Lett.* 28 (13), 2617–2620.
- Voiculescu, M., Usoskin, I., 2012. Persistent solar signatures in cloud cover: spatial and temporal analysis. *Environ. Res. Lett.* 7 (4), 044004.
- Voiculescu, M., Usoskin, I., Condurache-Bota, S., 2013, dec. Clouds blown by the solar wind. *Environ. Res. Lett.* 8 (4), 045032 <https://doi.org/10.1088/1748-9326/8/4/045032>. Retrieved from <https://doi.org/10.1088/1748-9326/8/4/045032>.
- Voiculescu, M., Usoskin, I.G., Mursula, K., 2006. Different response of clouds to solar input. *Geophys. Res. Lett.* 33 (21).
- Wagner, R., Yan, C., Lehtipalo, K., Duplissy, J., Nieminen, T., Kangasluoma, J., et al., 2017. The role of ions in new particle formation in the cloud chamber. *Atmos. Chem. Phys.* 17 (24), 15181–15197. <https://doi.org/10.5194/acp-17-15181-2017>. Retrieved from <https://acp.copernicus.org/articles/17/15181/2017/>.
- Walther, A., Heidinger, A.K., 2012. Implementation of the daytime cloud optical and microphysical properties algorithm (dcomp) in patmos-x. *J. Appl. Meteorol. Climatol.* 51 (7), 1371.